HAL
open science

A porous puckered V2O5 polymorph as new high performance cathode material for aqueous rechargeable zinc batteries

Daureen Batyrbekuly, Barbara Laïk, Jean Pierre Pereira-Ramos, Zhumabay Bakenov, Rita Baddour-Hadjean

To cite this version:

Daureen Batyrbekuly, Barbara Laïk, Jean Pierre Pereira-Ramos, Zhumabay Bakenov, Rita Baddour-Hadjean. A porous puckered V2O5 polymorph as new high performance cathode material for aqueous rechargeable zinc batteries. Journal of Energy Chemistry, 2021, 61, pp.459-468. 10.1016/j.jechem.2021.01.042 . hal-03139633

HAL Id: hal-03139633

https://hal.science/hal-03139633v1

Submitted on 7 Jul 2021

HAL is a multi-disciplinary open access archive for the deposit and dissemination of scientific research documents, whether they are published or not. The documents may come from teaching and research institutions in France or abroad, or from public or private research centers.

L'archive ouverte pluridisciplinaire **HAL**, est destinée au dépôt et à la diffusion de documents scientifiques de niveau recherche, publiés ou non, émanant des établissements d'enseignement et de recherche français ou étrangers, des laboratoires publics ou privés.

A porous puckered V_2O_5 polymorph as new high performance cathode material for aqueous rechargeable zinc batteries

Dauren Batyrbekuly[a,b], Barbara Laïk[a], Jean-Pierre Pereira-Ramos[a], Zhumabay Bakenov[b], Rita Baddour-Hadjean[a,*]

[a] *Institut de Chimie et des Matériaux Paris Est (ICMPE), UMR 7182 CNRS et Université Paris Est Créteil, 2 rue Henri Dunant, 94320 Thiais, France*
[b] *School of Engineering, National Laboratory Astana, Nazarbayev University, 53 Kabanbay Batyr Avenue, Astana 010000, Kazakhstan*

[*]Corresponding author.
E-mail address: baddour@icmpe.cnrs.fr (R. Baddour-Hadjean)

Abstract

Aqueous rechargeable zinc batteries are getting increasing attention for large-scale energy storage owing to their advantages in terms of cost, environmental friendliness and safety. Here, the layered puckered γ'-V_2O_5 polymorph with a porous morphology is firstly introduced as cathode for an aqueous zinc battery system in a binary Zn^{2+}/Li^+ electrolyte. The Zn||γ'-V_2O_5 cell delivers high capacities of 240 and 190 mAh g^{-1} at current densities of 29 and 147 mA g^{-1}, respectively, and remarkable cycling stability in the 1.6 V - 0.7 V voltage window (97% retention after 100 cycles at 0.15 A g^{-1}). The detailed structural evolution during first discharge-charge and subsequent cycling is investigated using X-ray diffraction and Raman spectroscopy. We demonstrate a reaction mechanism based on a selective Li insertion in the 1.6 V - 1 V voltage range. It involves a reversible exchange of 0.8 Li^+ in γ'-V_2O_5 and the same structural response as the one reported in lithiated organic electrolyte. However, in the extended 1.6 V - 0.7 V voltage range, this work puts forward a concomitant and gradual phase transformation from γ'-V_2O_5 to zinc pyrovanadate $Zn_3V_2O_7(OH)_2.2H_2O$ (ZVO) during

cycling. Such mechanism involving the *in-situ* formation of ZVO, known as an efficient Zn and Li intercalation material, explains the high electrochemical performance here reported for the Zn||γ'-V_2O_5 cell. This work highlights the peculiar layered-puckered γ'-V_2O_5 polymorph outperforms the conventional α-V_2O_5 with a huge improvement of capacity of 240 mAh g^{-1} vs 80 mAh g^{-1} in the same electrolyte and voltage window.

Keywords: Vanadium pentoxide, γ'-V_2O_5, Cathode, Aqueous zinc battery, High performance, Layered structure, Energy storage, Renewable energy

1. Introduction

Lithium ion batteries (LIBs) are known to provide the best option in terms of energy density and technical maturity to store renewable energy. However, LIBs large-scale energy storage systems have great limitations such as high cost and insufficient safety. In search of alternative batteries, aqueous rechargeable Zn-based batteries (ARZB) are attractive due to their low cost, safety and moderate toxicity. In addition, the high conductivity of the aqueous electrolyte made of Zn salts (*e.g.* 1M-3M $ZnSO_4$) allows a substantial gain on rate performance. While traditional alkaline electrolytes induce dendrite formation and byproducts, recent works have demonstrated the use of mild acidic electrolytes (pH ≈ 4) significantly improves the stability of metallic Zn anode [1–3].

Finding suitable cathode materials for ARZBs with high capacity, high operating voltage and long cycle life is actually a great challenge. Previous explorations of cathode materials mostly concern three main groups [4–6]: Prussian blue and analogues, manganese oxides and vanadium-based compounds that have been extensively investigated owing to the richness of layered structures in that family combined to the multiple oxidation states of vanadium [1,7–27]. Fast rate capability

and good capacity retention of 80-95% over a few hundred cycles with specific capacities mostly in the range 100-300 mAh g^{-1} have been reported for hydrated V-based compounds such as $Zn_{0.25}V_2O_5$. nH_2O [1], $V_2O_5.nH_2O$/RGO [7], V_2O_5 xerogel flakes [8], $V_3O_7.H_2O$ nanowires [9], $V_{10}O_{24}.12H_2O$ [10], $Mg_xV_2O_5.nH_2O$ [11], $K_2V_6O_{16}.2.7H_2O$ [12], $Ca_{0.25}V_2O_5.nH_2O$ [13], $Na_2V_6O_{16}.3H_2O$ [14], $Fe_5V_{15}O_{39}(OH).9.9H_2O$ nanosheets [15], $Zn_3V_2O_7(OH)_2.2H_2O$ [16] and hydrated porous δ-$Ni_{0.25}V_2O_5.nH_2O$ nanoribbons [17]. Anhydrous vanadium-based phases have also been investigated like VO_2 [18], $Zn_2V_2O_7$ [19], $NH_4V_4O_{10}$ [20], KV_3O_8, $K_2V_8O_{21}$ [21] and LiV_3O_8 [22].

In contrast to the abundant literature devoted to the vanadium oxide derivatives, very few works concern the conventional anhydrous α-V_2O_5 oxide. The reported papers [23–29] focus on the wide operating voltage windows 1.6 V-0.5 V, 1.5 V-0.3 V or 1.4 V-0.4 V involving the 2 electron-reaction or more. From a mechanistic point of view, zinc and water insertion are thought to be responsible for the formation of a $Zn_xV_2O_5$, nH_2O compound [25, 27] or a zinc pyrovanadate [27, 28] upon cycling. After an activation process over several cycles (fewer than ten, to a few dozen at most), highly stable capacities with scattered values in the range 220-470 mAh g^{-1} are achieved.

Recently, the use of a binary electrolyte of Li and Zn salts in mild acidic electrolyte attracted great interest, leading to the concept of rechargeable aqueous hybrid electrolyte, which involves two separate electrochemical redox processes on Zn anode and cathode, respectively. The electrolyte acts as conducting ions and cooperates with electrodes, ensuring efficient cyclability of Zn anode as well as reversible lithium insertion-extraction in the host cathodic material. Chen et al. proposed the first hybrid $Zn||ZnCl_2+LiCl||LiMn_2O_4$ system operating with high efficiency and long-term

cyclability [30]. In addition to $LiMn_2O_4$, other cathode materials like $LiFePO_4$ [31,32], $Li_3V_2(PO_4)_3$ [33], $LiVPO_4F$ [34], $LiNi_{1/3}Co_{1/3}Mn_{1/3}O_2$ [35], $LiMn_{0.8}Fe_{0.2}PO_4$ [36] have been investigated. High capacities in the range 100-130 mAh g^{-1} have been reported with good capacity retention upon cycling near 1.6/1.8V. A high rate capability is a common feature of such hybrid batteries with a 70-80% capacity retention at 4C.

We newly applied this concept of rechargeable aqueous hybrid batteries, using the conventional pristine α-V_2O_5 oxide as cathode material and Zn as anode in 2.5M Li_2SO_4 + 3.5M $ZnSO_4$ (pH = 4) binary electrolyte with a special emphasis on the structural mechanism involved upon discharge/charge process in the 1.6 V-0.8 V potential range (corresponding to the transfer of one-electron) [37]. The Zn||2.5M Li_2SO_4 + 3.5M $ZnSO_4$||α-V_2O_5 cell delivered capacity values about 136-125 mAh g^{-1} at C/20-C/5 rates (7.35-29.4 mA g^{-1}), respectively. At 1C (147 mA g^{-1}), a capacity of 80 mAh g^{-1} was outstandingly retained over more than 300 cycles. A detailed structural study by X-ray diffraction (XRD) and Raman spectroscopy allowed unravelling the peculiar response of the α-V_2O_5 layered host lattice. Strong similarities with the well-known structural changes reported in non-aqueous lithiated electrolytes were highlighted. The mitigated structural findings revealed a reaction mechanism mainly based on Li^+ intercalation but also suggested a possible cointercalation of Zn^{2+} cations or protons by the end of the discharge. The presence of a few zinc cations between the oxide layers were suggested to act as pillars stabilizing the structure upon cycling [37].

An exploratory approach for finding new advanced cathode materials in the vanadium oxide family consists in considering the interest of the various V_2O_5 polymorphs. Among them, γ'-V_2O_5 was recently proved to be of great interest as an insertion compound, with attractive electrochemical features for Li and Na-ion batteries [38–41]. In particular, the puckered layered lattice of γ'-V_2O_5 allows

reversible Li insertion in a higher voltage window by about 200 mV than α-V_2O_5 (3.6/3.5 V vs. 3.4/3.2 V vs. Li^+/Li). The structure of this polymorph consists of infinite ribbons made of VO_5 edge-sharing distorted pyramids leading to larger interlayer spacing (5.02 Å in γ'-V_2O_5 vs. 4.37 Å in α- V_2O_5), which enables an easier accommodation of guest cations.

However, in spite of such remarkable structural features, γ'-V_2O_5 phase has never been studied in an aqueous battery. In this work, the electrochemical and structural behaviour of γ'-V_2O_5 are depicted for the first time in an aqueous Zn||γ'-V_2O_5 battery using a binary 2.5M Li_2SO_4 + 3.5M $ZnSO_4$ electrolyte. Electrochemical performances are investigated in two different voltage ranges (1.6 V-1 V and 1.6 V-0.7 V) and the structural response of the cathode material is investigated by XRD and Raman spectroscopy.

2. Experimental

2.1. Synthesis

γ'-V_2O_5 was obtained by chemical oxidation of γ-LiV_2O_5 prepared by chemical lithiation of α-V_2O_5 under mild-temperature conditions. Further details can be found in [39]. A very fine powder of α-V_2O_5 with narrow particle size distribution was used as precursor, prepared using the polyol route [42]. The chemical reaction of α- V_2O_5 with LiI in excess (molar ratio 2:1) in acetonitrile leads to δ-LiV_2O_5. After drying at 70ºC, the δ-LiV_2O_5 powder was heat-treated at 300ºC for 3 h under vacuum in a Büchi furnace to form the distorted layered γ-LiV_2O_5 structure. The last step consists in extracting lithium ions from the interlayer spacing of γ-LiV_2O_5 without damaging the distorted host structure. This chemical oxidation reaction requires the use of the strong oxidizing agent NO_2BF_4 (molar ratio 1:4) in acetonitrile. The solution was stirred at room temperature for 4 h. The obtained powder was washed 4 times with acetonitrile

and acetone and then dried at 80 °C. The powder color changed from dark green to orange, which confirms the complete delithiation of the product. Electrochemical titration using galvanostatic oxidation and chemical redox titration confirmed the 5+ oxidation state of vanadium in γ'-V_2O_5.

2.2 Electrochemical tests

γ'-V_2O_5 positive electrodes were prepared by mixing 90 wt% of active material, 6 wt% polyvinylidene fluoride (PVDF, Kynar, HSV900) as a binder, 4 wt% carbon black (Ketjen Black International Co., Japan) as conductive agent dissolved in 1-methyl-2-pyrrolidinone (NMP, Sigma-Aldrich). The prepared slurry was casted on carbon paper (Alfa Aesar Co.), vacuum dried at 70 °C for 3 h and punched into disks of 8 mm in diameter. The mass loading of active material was around 6 mg cm^{-2}. Zinc foil (Goodfellow, USA) was used as both negative and reference electrodes. The electrolyte was prepared by dissolving 3.5M $ZnSO_4$ $7H_2O$ and 2.5M Li_2SO_4 in distilled water and according to previous pH optimizations [31], the pH was adjusted to 4 by titration with 0.5 mol L^{-1} H_2SO_4. Prepared electrolyte was bubbled with nitrogen gas (N_2) to remove dissolved oxygen. AGM (Absorptive Glass Mat NSG Corporation) was used as separator. The two-electrode cells were tested galvanostatically at various C rates (1 C corresponds to 147 mA g^{-1}) and by cyclic voltammetry (sweep rate 0.2 mV s^{-1}), using a VMP3 potentiostat/galvanostat (Bio-Logic Science Instrument Co.). The tests temperature was controlled at 20 °C. All potentials are reported in V vs. Zn/Zn^{2+}. The structural investigation of the Zn ‖ Li_2SO_4-$ZnSO_4$ ‖ γ'-V_2O_5 system was investigated by using a two-electrode split cell (MTI company). The cells were discharged or charged to the required composition at C/5 rate (29.4 mA g^{-1}). Then after disassembling the cell, the positive electrodes were rinsed in distilled water in order to

remove the traces of salt and separator, and then analyzed by XRD and Raman spectroscopy.

2.3. Characterizations

XRD measurements were carried out using a Panalytical X'pert pro diffractometer equipped with an X'celerator detector and a Co *K*α radiation (wavelength 1.7889 Å). All the diffraction patterns were collected with a 2θ step of 0.0167°. The Raman spectra were measured with a LaBRAM HR 800 (Jobin-Yvon-Horiba) Raman micro-spectrometer including Edge filters and equipped for signal detection with a back illuminated charge coupled device detector (Spex CCD) cooled by Peltier effect to 200 K. A He:Ne laser (632.8 nm) was used as the excitation source. The spectra were measured in back-scattering geometry. The resolution was about 0.5 cm^{-1}. A 50X LWD objective was used to focus the laser light on sample surface to a spot size of 1 μm^2. To avoid local heating of the sample, the power of the laser beam was adjusted to 0.2–0.5 mW with neutral filters of various optical densities. Raman spectra were recorded on ten different spots of each electrode to check the homogeneity. The pristine powder and the electrodes were characterized by scanning electron microscopy (SEM), Zeiss, Merlin-type microscope. Electron Dispersive X-ray (EDX) analysis was applied to determine the elemental composition together with SEM with an accelerating voltage of 10-15 kV

3. Results and discussion

3.1. Structural characterization of γ'-V_2O_5

SEM micrographs of the as-synthesized γ'-V_2O_5 powder (Fig. 1) reveals a homogeneous grain size distribution made of porous aggregates of small platelets in the range 100-500 nm. The XRD pattern of the as-synthesized γ'-V_2O_5 powder is shown in Fig. 2a. All the reflection lines can be indexed in an orthorhombic symmetry (JCPDS Card No. 01-085-2422, *Pnma* space group) leading to the following unit cell

parameters: a = 9.93(9) Å, b = 3.58(3) Å, c = 10.04(0) Å in agreement with literature data [41]. The Rietveld refinement of the XRD pattern (Fig. S1) confirms the presence of a pure and well-crystallized single phase. The layered structure of γ'-V_2O_5 is composed of infinite ribbons parallel to the b axis made of VO_5 edges-sharing distorted pyramids oriented alternatively up and down (inset in Fig.2a). These ribbons are linked to each other along the a-direction by one pyramid corner oxygen forming puckered layers perpendicular to the c-axis. The mean crystallite size estimated from diffraction peaks width is 90-100 nm.

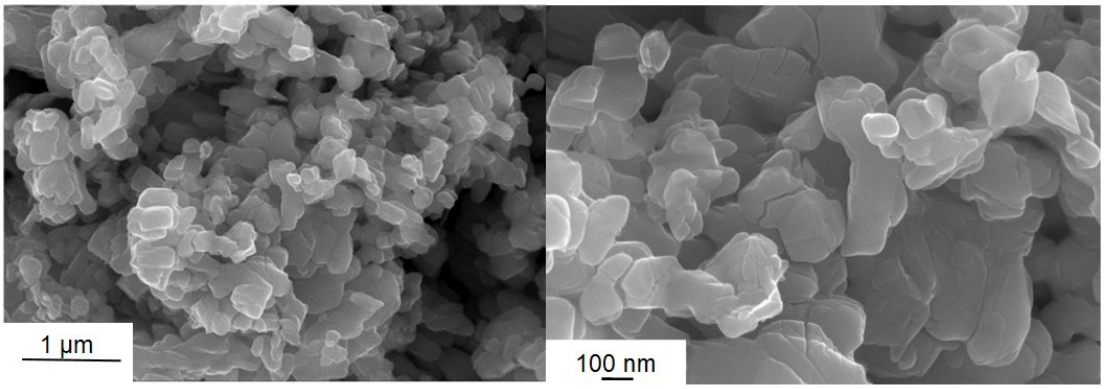

Fig. 1. SEM micrographs of as-prepared γ'-V_2O_5 powder.

The Raman spectrum of γ'-V_2O_5 is shown in Fig. 2b. The projection of the γ'-V_2O_5 structure along the b-crystallographic direction showing all the V-O contacts in the two non-equivalent vanadium environments (V_a, V_b) is shown in inset of Fig. 2b. This Raman fingerprint fully agrees with previous study [38]. The whole vibrations of the chains are identified as follows: bands at 1037, 1021 and 1003 cm^{-1} correspond to the stretching modes of the shortest V_a-O_{1a} and V_b-$O1_b$ bonds, bands at 752 and 603 cm^{-1} are related to the bond stretching vibrations localized within the V_a-O_3-V_b bridges. The stretching modes of the V_a-O_{2a}-V_a and V_b-O_{2b}-V_b bridges forming the rails of the ladders are observed at 722 and 694 cm^{-1}. Modes involving the V_a-O_{2a} and V_b-O_{2b} ladder step bonds (indicated by dashed line) are seen at 532 and 500 cm^{-1}. The lower

frequency modes at 92, 126, 138, 153, 171, 190, 238, 266, 282, 299, 349 and 390 cm^{-1} correspond to the complex distortions of the V_2O_5 ladders [38].

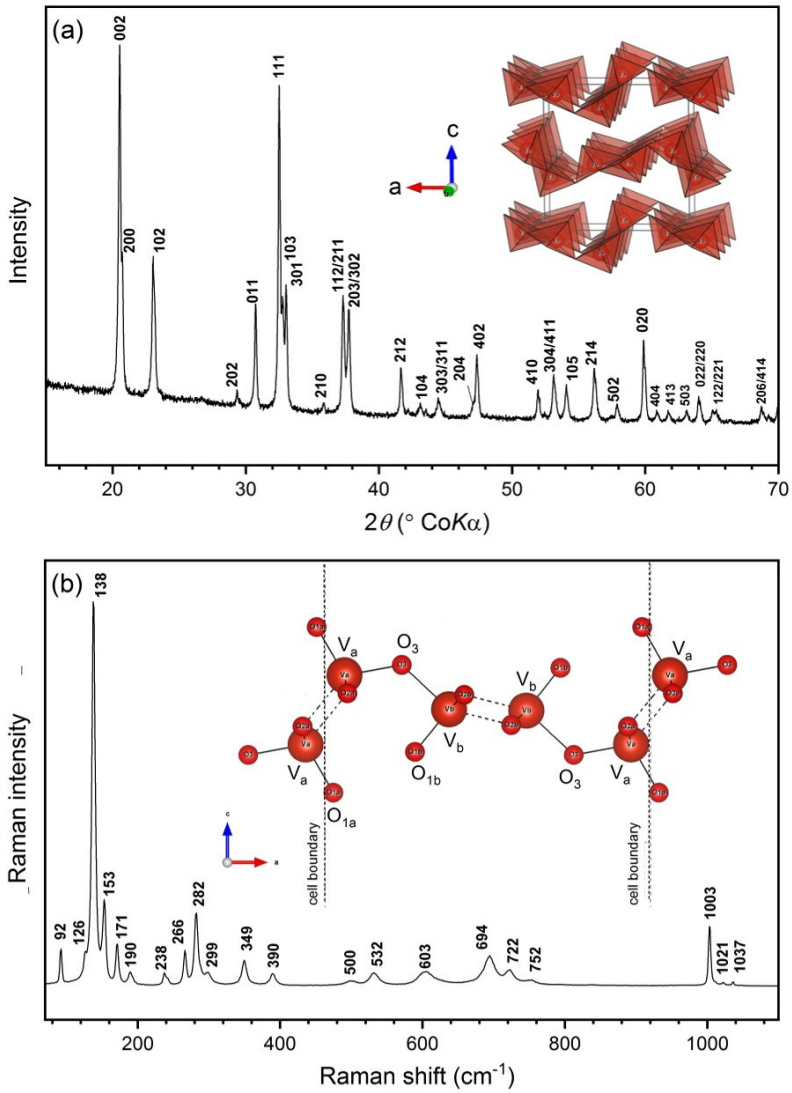

Fig. 2. (a) X-ray diffraction pattern of γ'-V_2O_5 powder. Inset: crystal structure of γ'- V_2O_5 (b) Raman spectrum of γ'-V_2O_5 powder. Inset: projection of the structure of γ'- V_2O_5 along the *b*-crystallographic direction showing all the V-O contacts. Dashed lines show V- O interchain contacts (ladder-step bonds)

3.2. Electrochemical study and structural mechanism in the 1.6 V- 1.0 V potential range

The first cyclic voltammetric curve of γ'-V_2O_5 (black curve in Fig. 3a) indicates that the electrochemical reaction is characterized by two distinct redox processes. Indeed, two cathodic peaks are observed at 1.32 V and 1.22 V with their corresponding reversible anodic peaks at 1.46 V and 1.31 V, respectively. The coulombic charge

involved upon cathodic scan corresponds to ≈ 0.8 F /mol of oxide and the same amount of electricity is engaged during the reverse scan, showing the excellent reversibility of electrochemical processes. The first discharge-charge profile of γ'-V_2O_5 at C/5 rate in the 1.6 V- 1.0 V potential range is shown in Fig. 3b. Similarly, the discharge curve exhibits two steps involving a total faradaic yield of 0.8 F mol^{-1} (specific capacity of 120 mAh g^{-1}). The voltage plateau at 1.38 V is related to the two sharp voltammetric peaks at 1.32/1.46 V and suggests a two-phase behavior, while the sloping curve centered near 1.27 V seems to indicate a single-phase redox process. A quantitative charge process is achieved, with only 30 mV hysteresis between discharge and charge, i.e. half that observed for α- V_2O_5. It is worth noting the higher operating voltage (≈+ 200 mV) of γ'-V_2O_5 compared with α-V_2O_5 (red dotted curves in Fig. 3), as observed in organic lithiated electrolyte [40], which outlines the interest of the puckered polymorph as cathode material in aqueous electrolyte. In addition, the present electrochemical fingerprint of γ'-V_2O_5 closely resembles that known in non-aqueous lithiated electrolyte [40]. This suggests a similar reaction mechanism is involved in binary Li_2SO_4/ $ZnSO_4$ electrolyte.

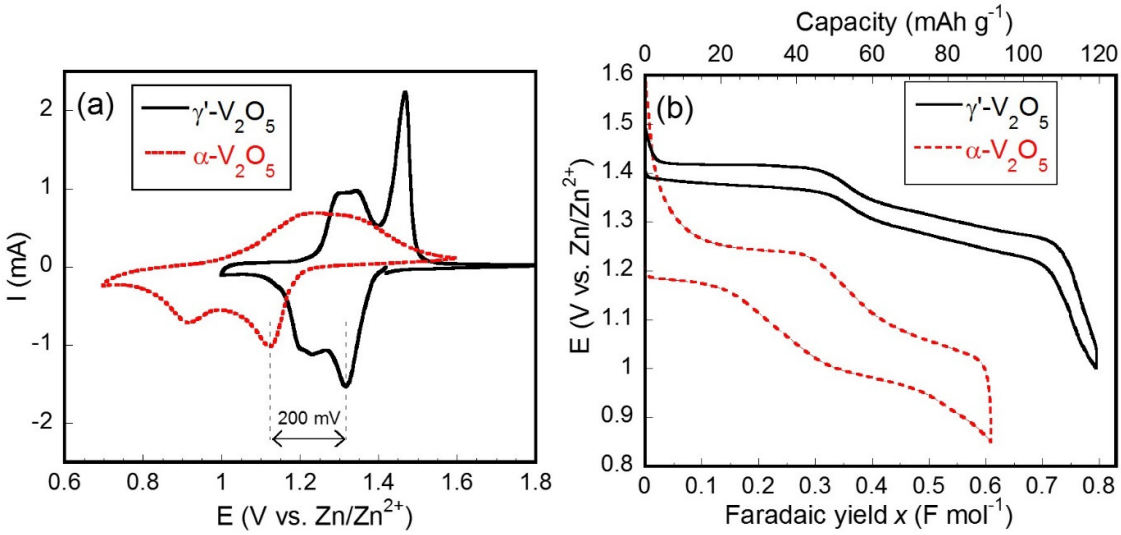

Fig. 3. (a) Cyclic voltammograms (scanning rate 0.2 mV s^{-1}) and (b) first galvanostatic cycles at C/5 rate of γ'-V_2O_5 (black curves) and α-V_2O_5 (red dotted curves).

To address this issue, we have investigated the structural response of γ'-V_2O_5 during the first discharge-charge cycle at C/5 in the 1.6 V- 1.0 V potential range, using XRD and Raman spectroscopy. The XRD patterns of reduced electrodes as a function of the faradaic yield x (in F mol^{-1}), $0 \leq x \leq 0.72$, are shown in Fig. 4. The XRD pattern of the pristine electrode ($x = 0$) shows the typical fingerprint of orthorhombic γ'-V_2O_5 (*Pnma* space group) with the unit cell parameters of the pristine powder (a = 9.94 Å, b = 3.58 Å, c = 10.04 Å). From the very first reduction rate (x = 0.1), a new set of 002, 102, 103 and 214 diffraction lines are detected at 19.95, 22.5, 32.0 and 55.3°, respectively, that coexist with those of the initial γ'-V_2O_5 material. This new set of lines is indexed in an orthorhombic symmetry (*Pnma* space group) and reveals the emergence of a lithiated γ-$Li_xV_2O_5$ phase. The same comment can be made for x = 0.2, with the new lines increasing at the expense of those related to the pristine compound. The shifts toward lower 2θ values for the 002, 102, 103, 104, 204, 105 and 214 reflections and to higher 2θ one for the 200 line clearly indicate an expansion in the c interlayer distance and a contraction in a parameter, respectively. Indeed, the unit cell parameters calculated for the reduced γ-$Li_xV_2O_5$ phases (x= 0.1; 0.2) are a = 9.83 Å, b = 3.59 Å, c = 10.34 Å. From x = 0.35, this trend is maintained: all the diffraction lines belong to the lithiated phase with a continuous shift of the 002 and 200 reflection lines toward higher and lower 2θ values, respectively, indicating a continuous expansion of c interlayer parameter and shrinkage in a parameter. In the $0.35 \leq x \leq 0.72$ composition range, the diffraction patterns show the existence of a single phase with cell parameters changing linearly with the depth of discharge. The unit cell parameters for the fully reduced γ-$Li_{0.72}V_2O_5$ electrode (a = 9.69 Å, b = 3.60 Å, c = 10.67 Å) match very well those reported for γ-$Li_1V_2O_5$ formed during electrochemical lithiation of γ'-V_2O_5 in non-aqueous lithiated electrolyte (a = 9.71 Å, b = 3.61 Å and c = 10.67 Å) [40]. It is

also worth noting the similarity of the unit cell variations vs. composition in aqueous and non-aqueous electrolytes [40]. Such findings are well consistent with a pure Li insertion reaction and enable us to rebut the hypothesis of water molecules, zinc or proton insertion into the γ'-V_2O_5 host lattice.

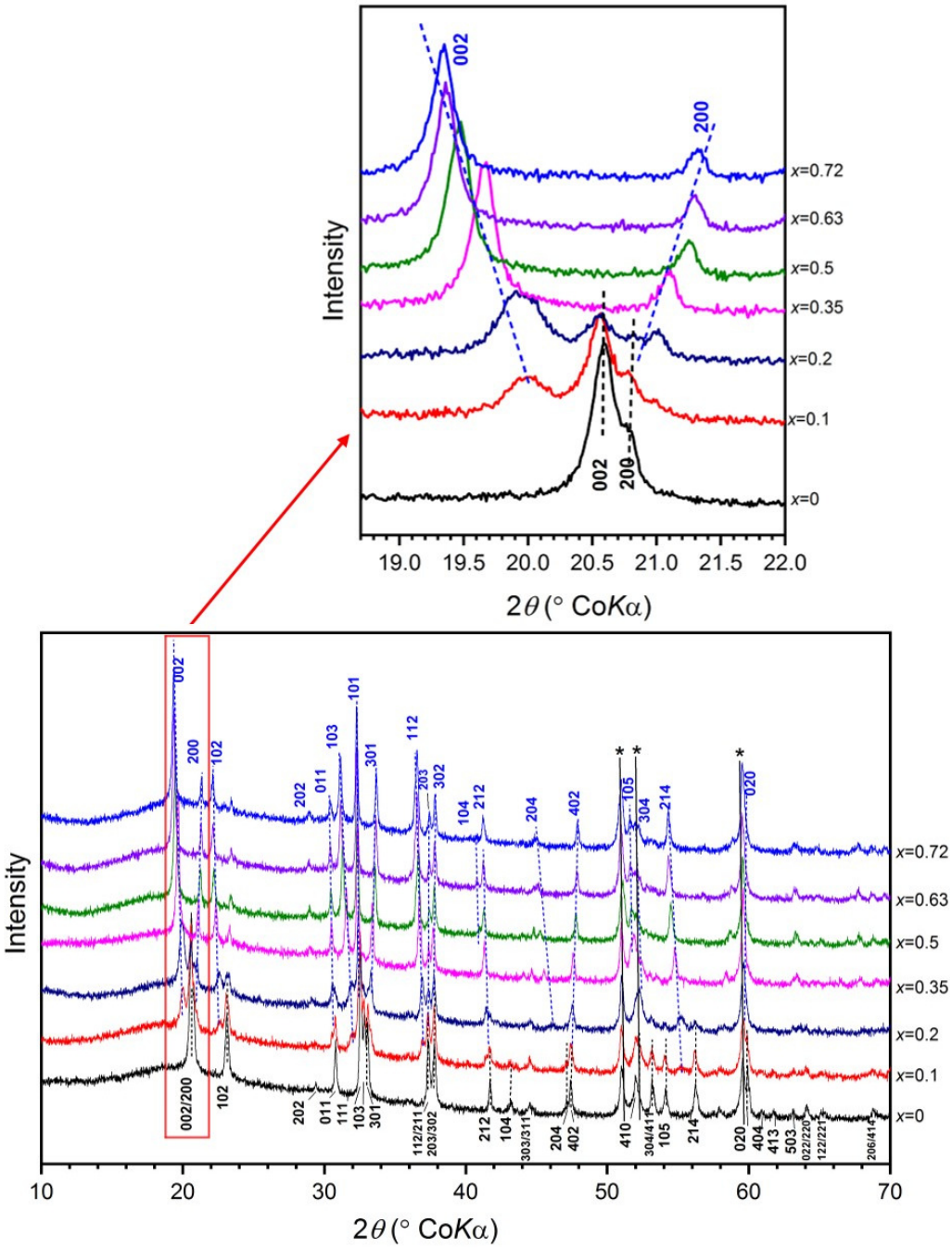

Fig. 4. X-ray diffraction patterns of reduced γ'-V_2O_5 electrodes during the first discharge at C/5 as a function of the faradaic yield x (F mol^{-1}). $0 \leq x \leq 0.72$. *: sample holder (stainless steel) reflections. 1.6 V - 1 V voltage window

The detailed lattice parameters evolutions as a function of x in γ-$Li_xV_2O_5$ during the first discharge ($0 \leq x \leq 0.72$) are depicted in Fig. 5. Two main domains clearly appear. First, a diphasic region for $0 < x < 0.35$ where γ'-V_2O_5 coexists with a lithiated phase γ-$Li_xV_2O_5$ characterized by a slight interlayer expansion of 3% (Fig. 5c) and a very low contraction of 1% along the *a* direction (Fig. 5a). On further reduction ($0.35 \leq x \leq 0.72$), a single-phase region is evidenced with a negligible *b* variation of 0.3% (Fig. 5b), a minor contraction in *a* parameter (1%) and a moderate expansion in *c* parameter (3%), showing the puckered layered arrangement of γ'-V_2O_5 is not altered upon Li insertion. The negligible change in *b* parameter is consistent with a Li diffusion occurring along the *b* direction.

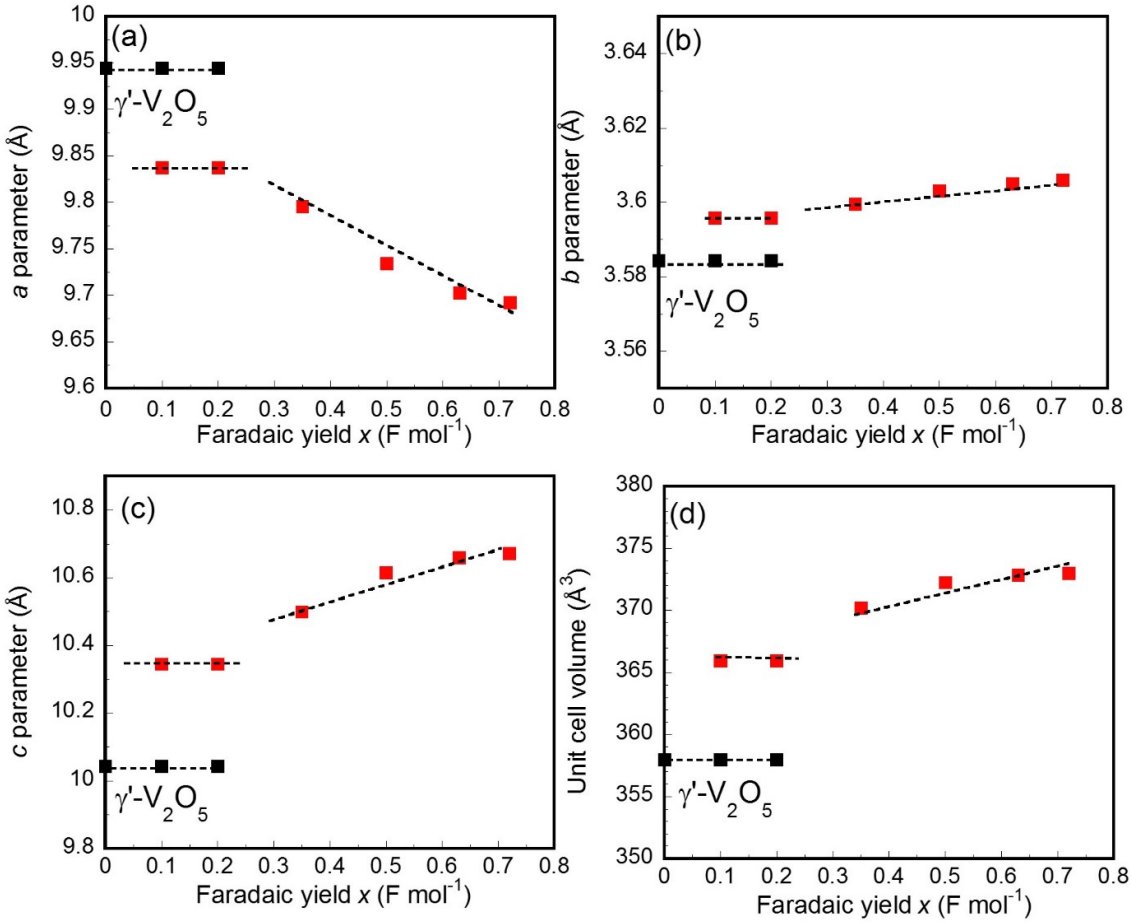

Fig. 5. Evolution of the unit cell parameters *a*, *b*, *c* and unit cell volume of reduced γ'-V_2O_5 electrodes during the first discharge at C/5 as a function of the faradaic yield x (F mol^{-1}). $0 \leq x \leq 0.72$. Black squares: γ'-V_2O_5; red squares: new phase.

The Raman spectra of reduced electrodes as a function of the faradaic yield x, $0 \leq x \leq 0.72$, are gathered in Fig. 6. As the reduction rate increases in the $0 < x \leq 0.5$ composition range, the Raman spectra undergo progressive changes in intensity or position while new bands are observed. These changes can be depicted as follows: the relative intensity of bands belonging to the pristine γ'-V_2O_5 material, at 91, 138, 153, 190, 238, 282, 299, 349, 500, 603, 694, 1003 and 1037 cm^{-1} gradually decreases up to their total disappearance for $x = 0.5$. At the same time, new peaks (indicated by blue open circles) belonging to the electroformed phase are detected, with increasing relative intensity as the reduction rate increases: at 990 cm^{-1} (from $x = 0.1$), 462 cm^{-1} (from $x = 0.35$), 100, 124, 331 and 966 cm^{-1} (from $x = 0.5$). Finally, three bands belonging to both systems are kept all along the reduction process but undergo continuous wavenumber shifts: 266 to 272 cm^{-1}, 722 to 731 cm^{-1}, 1021 to 1014 cm^{-1}. For $x = 0.35$, the Raman spectrum is modified, showing mostly the bands of the electroformed phase with only traces of the pristine oxide through the presence of low features at 138, 159, 171, 266, 282, 299 and 694 cm^{-1}. This is due to the very high Raman scattering cross section of γ'-V_2O_5 [38]. For $x = 0.5$, the Raman spectrum is characteristic of the pure new system with bands at 100, 124, 171, 272, 331, 374, 462, 531, 642, 731, 966, 990 and 1014 cm^{-1}. For $0.5 \leq x \leq 0.72$, the fingerprint of the new phase dominates the Raman spectrum. An ultimate feature appears at 642 cm^{-1} for the fully reduced sample while the 966 cm^{-1} peak increases in intensity. Such trends indicate the existence of a diphasic region in the composition range $0 < x < 0.35$, in which the pristine γ'-V_2O_5 phase disappears progressively while a new system emerges, followed by a single-phase region of the pure new system for $x \geq 0.35$. The Raman fingerprint of the electroformed phase matches perfectly that reported for γ-$Li_1V_2O_5$ formed during electrochemical lithiation of γ'-V_2O_5 in non-aqueous lithiated

electrolyte [40] as well as chemically synthesized γ-LiV_2O_5 [43]. The whole assignment of the Raman spectrum of the γ-LiV_2O_5 bronze can be found in [43]. Examination of the charged electrodes by XRD and Raman spectroscopy (Fig. S2) shows the complete restoration of the γ'-V_2O_5 host lattice after one discharge-charge cycle, both at the long-range order and atomic scale, with no extra peak or band related to the presence of another phase. Such findings explain the good electrochemical reversibility displayed in Fig. 3.

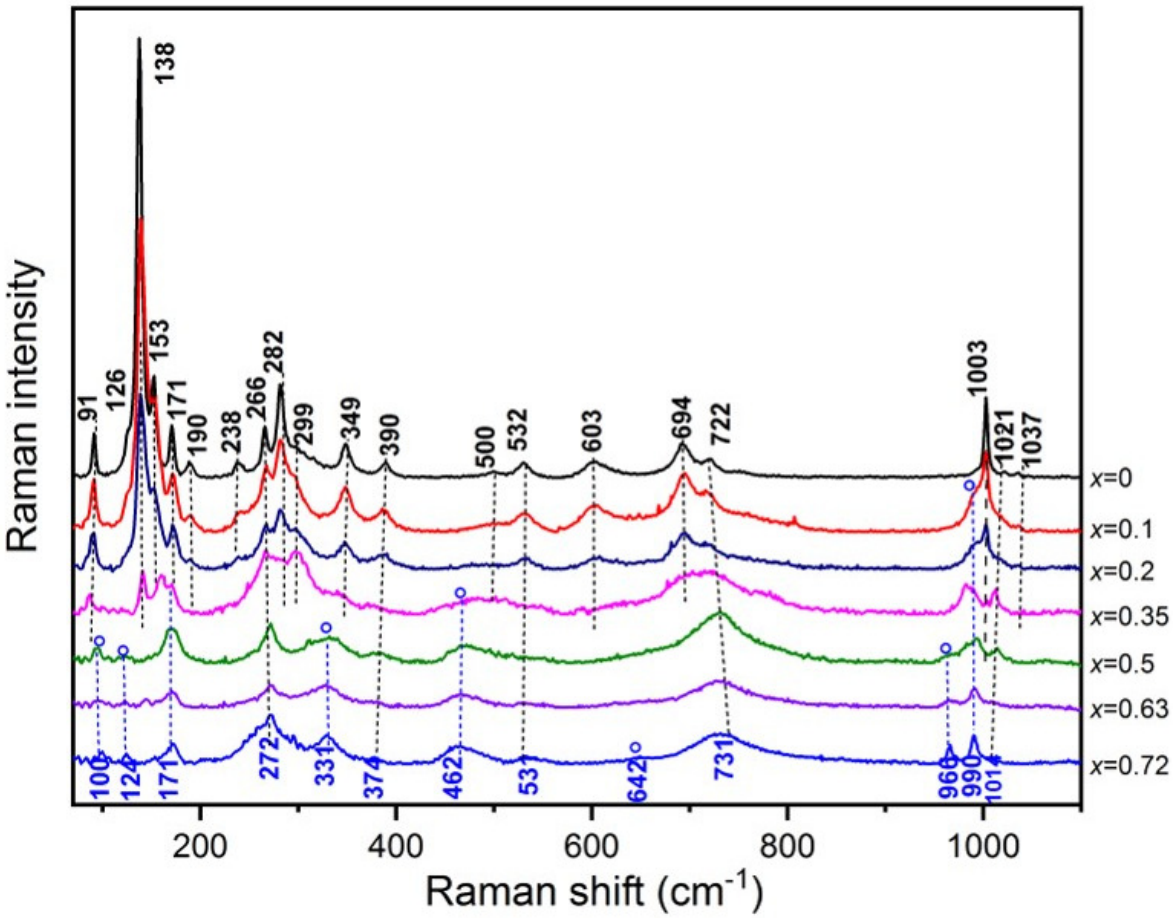

Fig. 6. Raman spectra of reduced γ'-V_2O_5 electrodes during the first discharge at C/5 as a function of the faradaic yield x (F mol^{-1}). $0 \leq x \leq 0.72$. 1.6 V - 1 V voltage window.

These structural data drawn from XRD and Raman spectroscopy reveal that γ'- V_2O_5 electrodes selectively intercalate Li^+ ions upon discharge. The nature of structural changes of the γ'-V_2O_5 host lattice as well their magnitude exclude any

participation of proton, zinc ions or water molecules. Instead, we highlight a reversible reaction mechanism, very similar to that reported in non-aqueous electrolyte [40], involving a diphasic domain for $0 < x < 0.35$ with coexistence of γ'-V_2O_5 and γ-$Li_{\approx 0.3}V_2O_5$, followed by a solid solution region γ-$Li_xV_2O_5$ for $0.35 \leq x \leq 0.72$.

Preliminary rate capability study indicates a promising behaviour since the specific capacity is little affected with increasing C rate (Fig. S3). Indeed the discharge capacity decreases from 120 mAh g^{-1} at C/5 to 105 and 95 mAh g^{-1} at 1C and 5C, respectively. In addition, the low hysteresis achieved between the charge and discharge, 60 mV at 1C and 100 mV at 5C, are quite remarkable. In spite of these promising performances, electrochemical experiments in the 1.6 V - 1 V voltage window do not allow to reach a specific capacity larger than 120 mAh g^{-1}, value that is much less than those usually reported for vanadium-based cathode materials [7–29]. In order to increase the available capacity, we have extended the voltage window by lowering the cutoff voltage to 0.7 V and investigated the electrochemical properties and related structural changes of γ'-V_2O_5 in this enlarged voltage range.

3.3. Electrochemical study and structural mechanism in the enlarged 1.6 V- 0.7 V potential range

The successive discharge-charge cycles of γ'-V_2O_5 at 1C rate are displayed in Fig. 7a. The first cycle exhibits the typical reversible fingerprint of γ'-V_2O_5 with two high voltage discharge steps at 1.36 V and 1.25 V followed by a potential drop, a total faradaic yield of 0.96 F mol^{-1} being involved. A careful examination of the first cycle shows however the presence of an additional ill-defined step near 0.9 V. The contribution of this lower voltage contribution increases with cycles, from about 0.13 F mol^{-1} for the first cycle to 0.3 F mol^{-1} for the second one and 0.65 F mol^{-1} for cycle 4, the total discharge capacity increasing significantly from 143 to 187 mAh g^{-1}.

At the same time, the contribution of the two high voltage steps decreases progressively to completely disappear for cycle 10, which exhibits a sloping voltage profile involving a capacity value of 185 mAh g^{-1}.

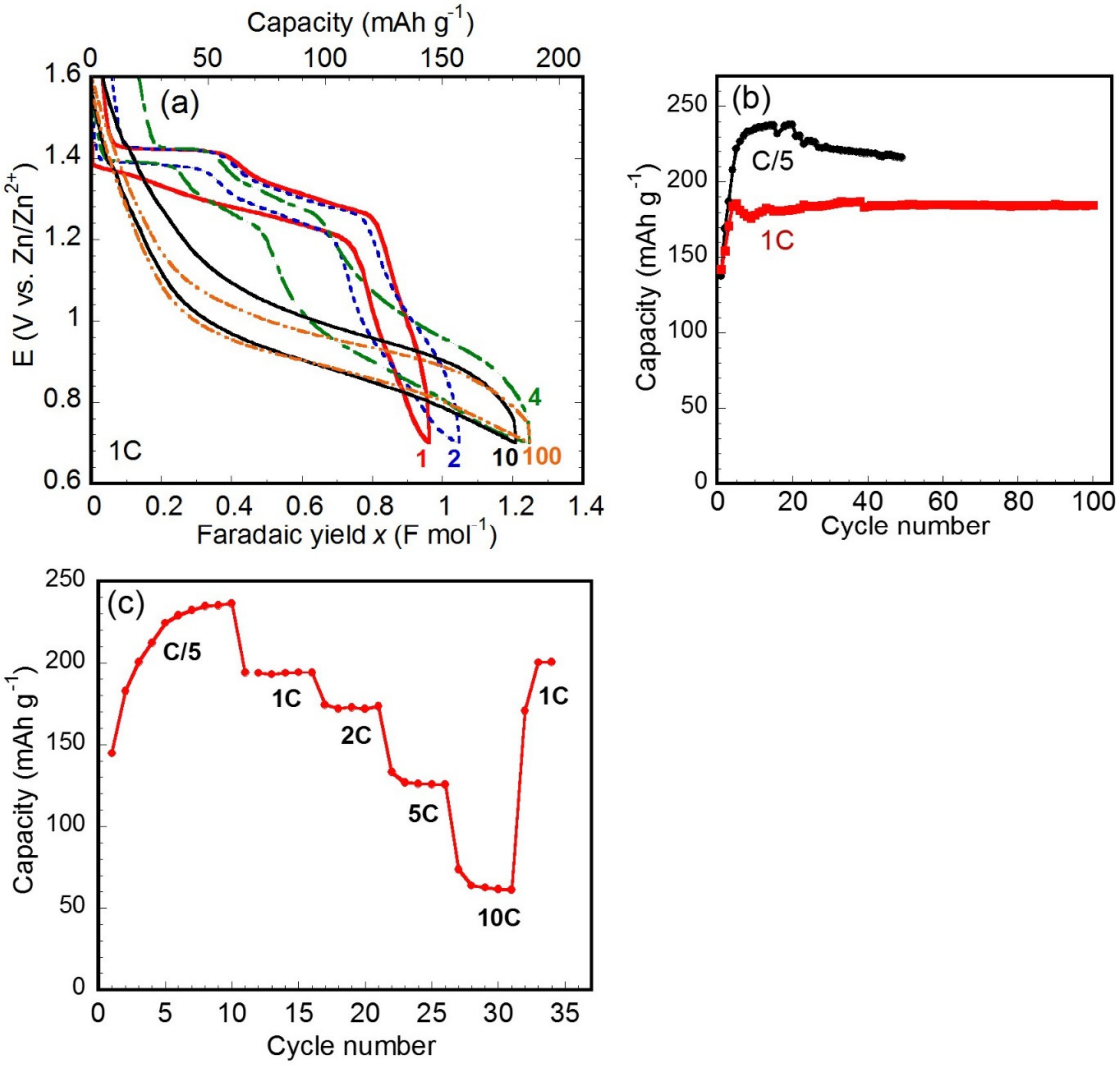

Fig. 7. Electrochemical performance of γ'-V_2O_5 in the extended 1.6 V - 0.7 V voltage window: (a) Discharge-charge cycles at 1C rate; (b) Evolution of the specific capacity as a function of the number of cycles at C/5 and 1C rates; (c) Rate capability study

Cycling tests (Fig. 7b) show a remarkable capacity retention of 97% at least over 100 cycles. A similar activation process is observed at C/5 rate (Fig. S4). Indeed, the capacity increases from 140 to 240 mAh g^{-1} along the ten first cycles, then stabilizes at 240 mAh g^{-1} over at least 50 cycles. This high stable capacity of 240 mAh g^{-1} competes

very well with previous values reported for V_2O_5 using only a Zn salt [23,26,28]. It is noteworthy the reproducible discharge profile displayed from cycle 10, with completely superimposed reversible charge process, does not exhibit anymore the typical Li insertion steps of γ'-V_2O_5. This suggests the lowering of the voltage window at 0.7 V induces a strong structural rearrangement. The redox process below 1 V involves a capacity that increases from 20 to 90 mAh g^{-1} during the five first cycles at 1C while the capacity contribution related to Li insertion in the upper voltage window (1.6 V - 1 V) decreases from 123 to 97 mAh g^{-1}. This trend is then confirmed up to cycle 10 with the 1.6 V - 1 V contribution still decreasing to only 50 mAh g^{-1} for the benefit of the low voltage part that reaches 120 mAh g^{-1} after the activation process. Since further lithiation is expected to occur around 1 V lower than the high voltage steps, i.e. at about 0.4 V [40], Zn^{2+} and/or proton insertion is probably involved below 1 V, leading to a progressive capacity gain and change in the discharge-charge profile during the first activation cycles.

The rate capability behaviour of γ'-V_2O_5 has been investigated in the C/5 -10C range, after performing an activation process of 10 cycles at C/5 (Fig. 7c and S5). Interesting capacities are reached: the stabilized capacity of 235 mAh g^{-1} at C/5 decreases moderately to 190 mAh g^{-1} at 1C, 170 mAh g^{-1} at 2C, still 130 mAh g^{-1} at 5C and 65 mAh g^{-1} at 10C. Even after sustaining high 10C rate, the cathode material is not damaged since the high capacity of about 200 mAh g^{-1} is recovered at 1C (Fig. 7c). Far superior cycling performance are found here for γ'-V_2O_5 compared to those recently reported for the conventional α-V_2O_5 form in the same binary Li/Zn electrolyte and same voltage range. Indeed, a stable capacity of only 80 mAh g^{-1} was achieved upon cycling α-V_2O_5 at 1C [37] against 180-190 mAh g^{-1} here for γ'-V_2O_5. This huge improvement in capacity value shows the porous puckered polymorph γ'-

V_2O_5 exhibits a more suitable structure towards zinc insertion, promoting then the electrochemical reaction. The promoting effect of a binary electrolyte on electrochemical performance of γ'-V_2O_5 in a Zn battery is highlighted in Fig. S6 showing a sharp capacity decrease in the pure $ZnSO_4$ electrolyte, with an available discharge capacity of only 50 mAh g^{-1} after 50 cycles while a fast capacity stabilization around 240 mAh g^{-1} over at least 50 cycles is observed using a hybrid electrolyte (Fig. 7b and S4).

The present capacities compete also well with those reported for α-V_2O_5 in binary $Zn(CF_3SO_3)_2$-LiTFSI "water in salt" electrolyte in the wider 1.6 V - 0.3 V voltage window [23]. A detailed comparison of γ'-V_2O_5 cycling behaviour with α-V_2O_5 properties is a difficult task. Indeed, the latter has been mainly investigated in $Zn(CF_3SO_3)_2$ or $ZnSO_4$ aqueous electrolytes, in various and larger cycling limits, using different electrode technologies and material morphologies, which may explain that scattered capacity values and occasionally contradictory data can be found in the range 200-400 mAh g^{-1} [24–26,28,29]. For instance a comparable capacity of 240 mAh g^{-1} is reported in 3M $ZnSO_4$ in the wide 1.4 V-0.4 V potential window [26] while higher values of 300-400 mAh g^{-1} are achieved in the 1.6 V-0.2/0.5 V potential range using porous nanofibers [28], ball-milled [25] and α- V_2O_5 microspheres [24]. Outstanding values of 400-500 mAh g^{-1} can be reached with ALD-deposited V_2O_5 layers on carbon paper but with a mass loading limited to 0.1 mg cm^{-2} [27].

To understand the peculiar electrochemical storage mechanism underlined by the discharge-charge profiles changes, we have carried out a structural study by XRD and Raman spectroscopy to provide information on the nature of the electroformed phases upon cycling of γ'-V_2O_5 in the 1.6 V - 0.7 V range. As shown in Fig. S7, the γ-type structure of the initial host lattice is kept on first discharge at 0.7 V. The shift toward

lower 2θ of the *00l* reflections (Fig. S7a) for the electrode discharged at 0.7 V reveals once again an expanded *c* interlayer parameter (10.67 Å vs. 10.03 Å for the initial material). The Raman spectrum of the discharged electrode displays also the characteristic bands of the lithiated γ-LiV_2O_5 structure (Fig. S7b). After one cycle, the initial structure of γ'-V_2O_5 is completely restored, both at the long range (Fig. S7a) and at the scale of chemical bond (Fig. S7b)**.** Furthermore, no extra peak or band related to the presence of another phase is detected. Such observations are consistent with the high electrochemical reversibility exhibited by the first cycle.

However, upon successive cycling tests, both XRD patterns and Raman analysis indicate the occurrence of an increasing disordering process and suggest a deep structural rearrangement upon cycling (Fig. 8) in line with the change observed in the cycling curves profiles (Fig. 7a and S4). Indeed, the XRD patterns (Fig. 8a) and Raman spectra (Fig. 8b) of discharged electrodes show a huge peak intensity decrease and Raman bands broadening with increasing cycling. This phenomenon takes place rapidly as only the 002, 102, 101, 301, 112 reflection lines of γ-$Li_xV_2O_5$ are still visible for the 6th discharge (Fig. 8a) whereas none of them can be detected for the 50th discharge. However, the presence of a new diffraction peak at 14.23° after 50 cycles (indicated by a cross in Fig. 8a) points to the formation of a new ill-crystallized phase that could correspond to trigonal $Zn_3V_2O_7(OH)_2.2H_2O$ pyrovanadate (ZVO, space group $P\bar{3}m1$, JCPDS 50-0570) [44,45]. Similar to V_2O_5, ZVO phase exhibits a layered structure built of zinc oxide layers separated by V-O-V pillars ($V_2O_7^{4-}$ groups), the water molecules randomly filling the large cavities [44,45]. The characteristic peak at 14.23° observed for the 50th discharge would then correspond to the most intense *001*

reflection of ZVO, giving an interlayer *c* parameter of 7.3 Å, in good accord with the values reported in previous studies [16,44–46].

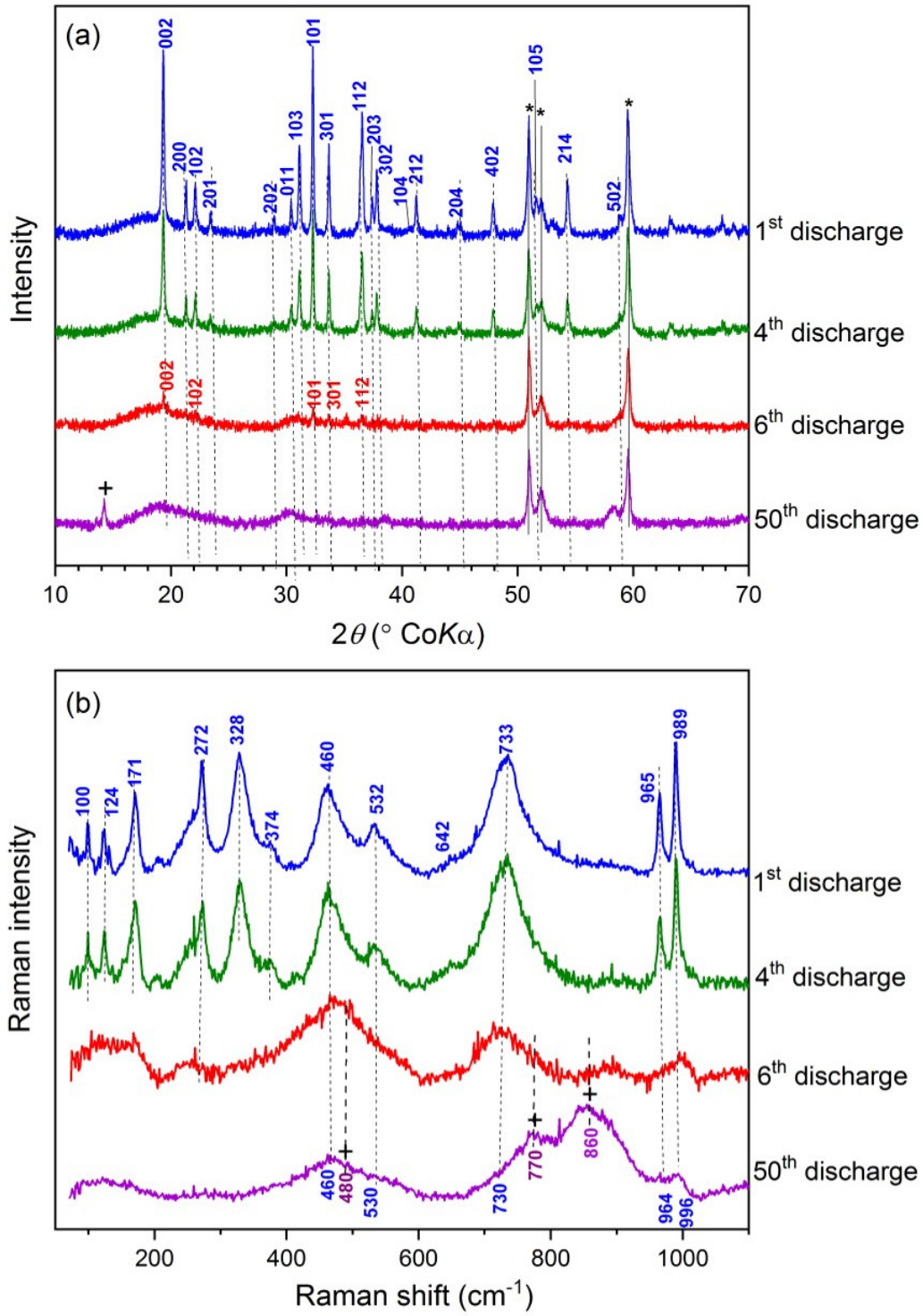

Fig. 8. (a) XRD patterns and (b) Raman spectra of γ'-V_2O_5 discharged electrodes upon cycling. *: sample holder (stainless steel) reflections. **+**: new phase. 1C rate. 1.6 V-0.7 V voltage window.

The Raman spectra of discharged electrodes also point to a significant amorphization process with cycling (Fig. 8b). While the typical fingerprint of γ-LiV_2O_5 is nicely distinguished for the 4th discharge, a low intensity spectrum is displayed for the 6th discharge, with broad features centered at 460, 530, 730 and 996 cm^{-1} indicating the presence of disordered γ-LiV_2O_5. For the 50th discharge, the Raman spectrum still points to the presence γ-LiV_2O_5 (characteristic peaks at 460, 964 and 996 cm^{-1} indicated in blue color), however coexisting with a new phase giving well visible bands at 770 and 860 cm^{-1}. Such phase is likely to correspond to ZVO, characterized by Raman modes at 482, 791 and 876 cm^{-1} [46]. Hence, the bands observed at 770 and 860 cm^{-1} after 50 cycles (see crosses in Fig. 8b) are likely to correspond to the most intense V-O stretching vibrations localized in VO_4 and VO_3 polyhedra in ZVO. The lower intensity Zn-O vibration expected at 482 cm^{-1} is barely visible in the wide intense 460 cm^{-1} broad feature of A_g symmetry assigned to the stretching $\nu(V_b\text{-}O_3)$ mode localized within the $V_a\text{-}O_3\text{-}V_b$ bridges in γ-$Li_xV_2O_5$ [43].

The increasing disordering process upon cycling is also observable on the charged electrodes. Indeed, the typical *hkl* reflections of γ'-V_2O_5 have practically disappeared after 6 cycles and are no more discernable after 50 cycles (Fig. S8a) while the occurrence of electroformed ZVO manifests itself again through the observation of a 001 reflection at 14.4°. At the level of the chemical bond, the well-defined Raman bands of γ'-V_2O_5 merge into broad bands after 6 cycles, located at ca. 150, 300, 750 and 1000 cm^{-1} (Fig. S8b) while new components at 480 and 770 cm^{-1} (indicated by crosses) arise from cycle 6, revealing the presence of ZVO phase coexisting with disordered γ'-V_2O_5.

This electrochemical and structural study suggests deep structural changes take place upon cycling γ'-V_2O_5 in the 1.6 V - 0.7 V voltage range. While an exclusive Li

insertion process is clearly demonstrated when the discharge is limited to 1 V, another mechanism responsible for a fast disordering process and involving Zn participation is observed in the lower 1 V- 0.7 V voltage range. XRD and Raman analysis both converge toward the formation of ZVO as new electroactive phase responsible for the capacity gain, the high capacity and the excellent cyclability highlighted in this work. This gradual phase transformation from γ'-V_2O_5 to ZVO is probably promoted by a chemical reaction between the positive electrode and the aqueous hybrid electrolyte according to Eq. (1) and Eq. (2) [27]:

$$V_2O_5 + 3H_2O \leftrightarrows 2VO_2(OH)_2^- + 2H^+ \quad (1)$$

$$2VO_2(OH)_2^- + 3Zn^{2+} + 3H_2O \leftrightarrows Zn_3V_2O_7(OH)_2.2H_2O + 4H^+ \quad (2)$$

Hence, the mechanism involved during discharge-charge in the present binary electrolyte is illustrated in Eq. (3) and Eq. (4):

In the 1.6 V - 1 V voltage range ($x < 1$):

$$\gamma'\text{-}V_2O_5 + xe^- + xLi^+ \leftrightarrows \gamma\text{–}Li_xV_2O_5 \quad (3)$$

In the 1 V - 0.7 V voltage range (after activation):

$$ZVO + (x+2y)e^- + xLi^+ + yZn^{2+} \leftrightarrows Li_xZn_yZVO \quad (4)$$

Previous works have reported ZVO as promising intercalation cathode for aqueous ZIB [16] and non-aqueous Li-ion battery [46]. Such findings are ascribed to the open framework with large interlayer spacing of ZVO (0.74 nm *vs* 0.43 nm for hydrated ionic radius of Zn^{2+}), providing an ideal pathway for guest species intercalation.

Even when all structural data on V_2O_5 derived electrodes deal with cycling properties obtained in wider voltage ranges using a lower cutoff voltage (0.2 V - 0.4 V) and only a Zn salt (3M $ZnSO_4$ or $Zn(CF_3SO_3)_2$), some common features exist with the present study. Indeed, a phase transformation is often reported upon successive discharge-charge cycles involving the hydrated layered phases $H_2V_3O_8$ [26] or

$Zn_xV_2O_5$ nH_2O [25] while other studies indicate the predominant role of $Zn_3V_2O_7(OH)_2.2H_2O$ [27,28]. The present structural analysis clearly demonstrates a fast transformation of γ'-V_2O_5 from the first cycle. XRD and Raman data show a more complex mechanism than in pure Zn based electrolytes since Li ions can still participate to the electrochemical process of layered ZVO phases whatever their composition. However, the active material obtained after capacity stabilization is made of disordered γ'-V_2O_5 and ZVO. It can be argued that longer cycling experiments would allow a complete conversion of the initial crystalline γ'-V_2O_5 phase into ZVO.

Additional supporting evidence to the phase transformation is provided by EDX measurements performed for electrodes discharged to 0.7 V (1st, 4th, 6th and 50th discharge). Table 1 shows that the discharged product continuously enriches itself with Zn ions with cycling, as revealed by the significant increase of the Zn/V ratio. Such a finding supports a phase transformation from γ'-V_2O_5 to ZVO, as recently evidenced in 3M $Zn(CF_3SO_3)_2$ electrolyte for Atomic Layer Deposited derived α-V_2O_5 [27] and α-V_2O_5 nanofibers [28]. The maximum Zn/V value of 0.62 associated to a faradaic yield of 1.2 e^- /mol of V_2O_5 discards a pure Zn insertion reaction leading to the $Zn_xV_2O_5$ bronze. Moreover, this value does not meet either the expected Zn/V ratio of 1.5 in ZVO, which can be understood assuming the coexistence of disordered γ'-V_2O_5 with ZVO in the electrodes, in which Li ions can still be reversibly inserted.

Table 1. Zn/V ratios determined from EDX in discharged γ'-V_2O_5 electrodes at 0.7 V. Cycle rate 1C.

Discharge number	Zn/V
1	0.16
4	0.27
6	0.51
50	0.62

4. Conclusions

In this work, we present the layered-puckered γ'-V_2O_5 as a prospective cathode for zinc-ion batteries in a binary 3.5M $ZnSO_4$ + 2.5M Li_2SO_4 electrolyte. After an activation process of a few cycles, high and stable capacities of 240 mAh g^{-1} and 190 mAh g^{-1} are achieved in the 1.6 V- 0.7 V potential window at C/5 and 1C rate, respectively. These capacities outperform those reported for the conventional α- V_2O_5 oxide in the same electrolyte. The detailed structural evolution during first discharge-charge and subsequent cycling in two different voltage ranges (1.6 V - 1 V and 1.6 V - 0.7 V) is investigated using XRD and Raman spectroscopy. We show the occurrence of selective lithium intercalation in the 1.6 V - 1 V voltage window, with a reversible exchange of 0.8 Li^+ in γ'-V_2O_5 inducing the same structural response as the one reported in lithiated organic electrolyte while a concurrent reaction involving zinc ions takes place concomitantly in the extended 1.6 V- 0.7 V range.

A gradual phase transformation from γ'-V_2O_5 to zinc pyrovanadate $Zn_3V_2O_7(OH)_2.2H_2O$ during cycling is strongly supported by XRD, Raman and EDX analysis. This work highlights the benefit provided by the peculiar layered-puckered γ'-V_2O_5 against conventional α-V_2O_5 with a huge improvement of capacity of 240 mAh g^{-1} vs 80 mAh g^{-1} at C/5 in the same voltage window. Further optimization of cycling properties are under investigation by lowering the cut-off voltage to 0.3 V.

Declaration of competing interests

The authors declare that they have no known competing financial interests or personal relationships that could have appeared to influence the work reported in this paper.

Acknowledgments

One of the authors wishes to thank the Ministry of Education and Science of Kazakhstan (grant number AP05136016-ZRABS), French Embassy in Astana, Kazakhstan and Campus France for financial support. All the authors thank Dr. Nicolas Emery (ICMPE-CNRS) for assistance in refinement of XRD data.

References

[1] D. Kundu, B.D. Adams, V. Duffort, S.H. Vajargah, L.F. Nazar, Nat. Energy 1 (2016) 16119.
[2] H. Pan, Y. Shao, P. Yan, Y. Cheng, K.S. Han, Z. Nie, C. Wang, J. Yang, X. Li, P. Bhattacharya, Nat. Energy 1 (2016) 16039.
[3] F. Wan, L. Zhang, X. Dai, X.Wang, Z. Niu, J. Chen, Nat. Commun. 9 (2018) 1656.
[4] A. Konarov, N. Voronina, J.H. Jo, Z. Bakenov, Y.-K. Sun, S.-T. Myung, ACS Energy Lett. 3 (2018) 2620–2640.
[5] J. Ming, J. Guo, C. Xia, W. Wang, H.N. Alshareef, Mater. Sci. Eng.: R: Reports 135 (2019) 58–84.
[6] G. Fang, J. Zhou, A. Pan, S. Liang, ACS Energy Lett. 3 (2018) 2480–2501.
[7] M. Yan, P. He, Y. Chen, S. Wang, Q. Wei, K. Zhao, X. Xu, Q. An, Y. Shuang, Y. Shao, Adv. Mater. 30 (2018) 1703725.
[8] Y. Li, P. Xu, J. Jiang, J. Yao, B. Huang, J. Yang, Mater. Today Commun. (2020) 101849.
[9] P. He, Y. Quan, X. Xu, M. Yan, W. Yang, Q. An, L. He, L. Mai, Small 13 (2017) 1702551.
[10] T. Wei, Q. Li, G. Yang, C. Wang, Electrochim. Acta 287 (2018) 60–67.
[11] F. Ming, H. Liang, Y. Lei, S. Kandambeth, M. Eddaoudi, H.N. Alshareef, ACS Energy Lett. 3 (2018) 2602–2609.
[12] B. Sambandam, V. Soundharrajan, S. Kim, M.H. Alfaruqi, J. Jo, S. Kim, V. Mathew, Y.-K Sun, J. Kim, J. Mater. Chem. A 6 (2018) 15530–15539.
[13] C. Xia, J. Guo, P. Li, X. Zhang, H.N. Alshareef, Angew. Chemie Int. Ed. 57 (2018) 3943–3948.
[14] V. Soundharrajan, B. Sambandam, S. Kim, M.H. Alfaruqi, D.Y. Putro, J. Jo, S. Kim, V. Mathew, Y.-K. Sun, J. Kim, Nano Lett. 18 (2018) 2402–2410.
[15] Z. Peng, Q. Wei, S. Tan, P. He, W. Luo, Q. An, L. Mai, Chem. Commun. 54 (2018) 4041–4044.
[16] C. Xia, J. Guo, Y. Lei, H. Liang, C. Zhao, H.N. Alshareef, Adv. Mater. 30 (2017) 1705580.
[17] J. Li, K. McColl, X. Lu, S. Sathasivam, H. Dong, L. Kang, Z. Li, S. Zhao, A.G. Kafizas, R. Wang, D.J.L. Brett, P.R. Shearing, F. Corà, G. He, C. J. Carmalt, I.P. Parkin, Adv. Energy Mater. 10 (2020) 2000058.
[18] T. Wei, Q. Li, G. Yang, C. Wang, J. Mater. Chem. A 6 (2018) 8006–8012.
[19] B. Sambandam, V. Soundharrajan, S. Kim, M.H. Alfaruqi, J. Jo, S. Kim, V. Mathew, Y.-K Sun, J. Kim, J. Mater. Chem. A 6 (2018) 3850–3856.
[20] G. Yang, T. Wei, C. Wang, ACS Appl. Mater. Interfaces 10 (2018) 35079–35089.
[21] B. Tang, G. Fang, J. Zhou, L. Wang, Y. Lei, C. Wang, T. Lin, Y. Tang, S. Liang, Nano Energy 51 (2018) 579–587.

[22] M.H. Alfaruqi, V. Mathew, J. Song, S. Kim, S. Islam, D.T. Pham, J. Jo, S. Kim, J.P. Baboo, Z. Xiu, Chem. Mater. 29 (2017) 1684–1694.
[23] P. Hu, M. Yan, T. Zhu, X. Wang, X. Wei, J. Li, L. Zhou, Z. Li, L. Chen, L. Mai, ACS Appl. Mater. Interfaces 9 (2017) 42717–42722.
[24] P. Hu, T. Zhu, J. Ma, C. Cai, G. Hu, X. Wang, Z. Liu, L. Zhou, L. Mai, Chem. Commun. 55 (2019) 8486–8489.
[25] N. Zhang, Y. Dong, M. Jia, X. Bian, Y. Wang, M. Qiu, J. Xu, Y. Liu, L. Jiao, F. Cheng, ACS Energy Lett. 3 (2018) 1366–1372.
[26] J. Zhou, L. Shan, Z. Wu, X. Guo, G. Fang, S. Liang, Chem. Commun. 54 (2018) 4457–4460.
[27] Y. Lu, T. Zhu, W. van den Bergh, M. Stefik, K. Huang, Angew. Chem. Int. Ed. 59 (2020) 17004–17011.
[28] X. Chen, L. Wang, H. Li, F. Cheng, J. Chen, J. Energy Chem. 38 (2019) 20–25.
[29] W. Zhou , J. Chen, M. Chen, X. Xu, Q.Tian, J. Xu, C.P. Wong, RSC Adv. 9 (2019) 30556–30564.
[30] J.Yan, J. Wang, H. Liu, Z. Bakenov, D. Gosselink, P. Chen, J. Power Sources 216 (2012) 222–226.
[31] N. Yesibolati, N. Umirov, A. Koishybaya, M. Omarova, I. Kurmanbayeva, Y. Zhang, Y. Zhao, Z. Bakenov, Electrochim. Acta 152 (2014) 505–511.
[32] G. Yuan, J. Bai, T.N.L. Doan, P. Chen, Mater. Lett. 158 (2015) 248–251.
[33] H.B. Zhao, C.J. Hu, H.W. Cheng, J.H. Fang, Y.P. Xie, W.Y. Fang, T.N.L. Doan, T.K.A. Hoang, J.Q. Xu, P. Chen, Sci. Rep. 6 (2016) 1–10.
[34] Z. Liu, Q. Yang, D. Wang, G. Liang, Y. Zhu, F. Mo, Z. Huang, X. Li, L. Ma, T. Tang, Z. Lu, C. Zhi, Adv. Energy Mater. 9, 1–12 (2019).
[35] F. Wang, Y. Liu, X. Wang , Z. Chang,Y. Wu, R. Holze, ChemElectroChem 2 (2015) 1024–1030.
[36] J. Zhao, Y. Li, X. Peng, S. Dong, J. Ma, G. Cui, L. Chen, Electrochem. commun. (2016) 69, 6–10.
[37] D. Batyrbekuly, S. Cajoly, B. Laïk, J.-P. Pereira-Ramos, N. Emery, Z. Bakenov, R. Baddour-Hadjean, ChemSusChem 13 (2020) 724–731.
[38] R. Baddour-Hadjean, M.B. Smirnov, V.Y. Kazimirov, K.S. Smirnov, J.-P. Pereira-Ramos, J. Raman Spectrosc. 46 (2015) 406–412.
[39] N. Emery, R. Baddour-Hadjean, D. Batyrbekuly, B. Laïk, Z. Bakenov, J.-P. Pereira-Ramos, Chem. Mater. 30 (2018) 5305–5314.
[40] R. Baddour-Hadjean, M. Safrany Renard, J.-P. Pereira-Ramos, Acta Mater. 165 (2019) 183–191.
[41] M. Safrany Renard, N. Emery, R. Baddour-Hadjean, J.-P. Pereira-Ramos, Electrochim. Acta 252 (2017) 4–11.
[42] I. Mjejri, A. Rougier, M. Gaudon, Inorg. Chem. 56 (2017) 1734–1741.
[43] M.B. Smirnov, E.M. Roginskii, V.Y. Kazimirov, K.S. Smirnov, R. Baddour-Hadjean, J.-P. Pereira-Ramos, V.S. Zhandun, J. Phys. Chem. C 119 (2015) 20801-–20809. https://doi.org//10.1021/acs.jpcc.5b05540.
[44] P.Y. Zavalij, F. Zhang, M.S. Whittingham, Acta Cryst. C 53 (1997) 1738-1739.
[45] T. Chirayil, P. Y. Zavalij, M.S. Whittingham, Chem. Mater. 10 (1998) 2629–2640.
[46] S. Ni, G. Zhou, S. Li, X. Wang, Q. Pan, F. Yang, D. He, Mater. Lett. 63 (2009) 2459–2461.

Graphical Abstract

γ'-V_2O_5, which undergoes a transition toward zinc pyrovanadate (ZVO) below 1 V during first cycles and dual Li^+/Zn^{2+} insertion/extraction in the layered hosts thereafter, is a new attractive cathode material for ARZB.

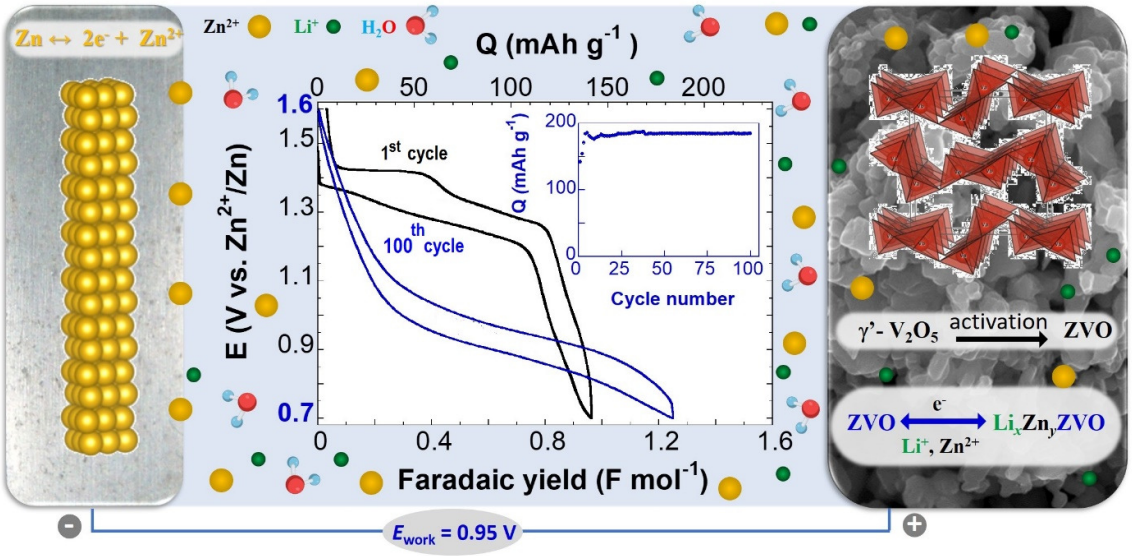

Figure captions

Figure 1. SEM micrographs of as-prepared γ'-V_2O_5 powder

Figure 2. (a) X-ray diffraction pattern of γ'-V_2O_5 powder. Inset: crystal structure of γ'- V_2O_5 (b) Raman spectrum of γ'-V_2O_5 powder. Inset: projection of the structure of γ'- V_2O_5 along the *b*-crystallographic direction showing all the V-O contacts. Dashed lines show V- O interchain contacts (ladder-step bonds)

Figure 3. (a) Cyclic voltammograms (scanning rate 0.2 mV s^{-1}) and (b) First galvanostatic cycles at C/5 rate of γ'-V_2O_5 (black curves) and α-V_2O_5 (red dotted curves)

Figure 4. X-ray diffraction patterns of reduced γ'-V_2O_5 electrodes during the first discharge at C/5 as a function of the faradaic yield x (F mol^{-1}). $0 \leq x \leq 0.72$. *: sample holder (stainless steel) reflections. 1.6 V - 1 V voltage window

Figure 5. Evolution of the unit cell parameters *a*, *b*, *c* and unit cell volume of reduced γ'-V_2O_5 electrodes during the first discharge at C/5 as a function of the faradaic yield x (F mol^{-1}). $0 \leq x \leq 0.72$. Black squares: γ'-V_2O_5; red squares: new phase

Figure 6. Raman spectra of reduced γ'-V_2O_5 electrodes during the first discharge at C/5 as a function of the faradaic yield x (F mol^{-1}). $0 \leq x \leq 0.72$. 1.6 V - 1 V voltage window

Figure 7. Electrochemical performance of γ'-V_2O_5 in the extended 1.6 V - 0.7 V voltage window: (a) Discharge-charge cycles at 1C rate; (b) Evolution of the specific capacity as a function of the number of cycles at C/5 and 1C rates; (c) Rate capability study

Figure 8. (a) XRD patterns and (b) Raman spectra of γ'-V_2O_5 discharged electrodes upon cycling. *: sample holder (stainless steel) reflections. **+**: new phase. 1C rate. 1.6 V- 0.7 V voltage window

Appendix A: Supplementary data

Figure S1. Rietveld refinement of γ'-V_2O_5 XRD pattern

Figure S2. (a) XRD patterns and (b) Raman spectra of initial γ'-V_2O_5 electrode and after one discharge-charge cycle. C/5 rate. 1.6 V - 1 V voltage window. Stars correspond to the sample holder (stainless steel) reflections

Figure S3. Influence of the C rate on discharge-charge curves of γ'-V_2O_5. 1.6 V - 1 V voltage window. 2.5M Li_2SO_4-3.5M $ZnSO_4$ electrolyte

Figure S4. Discharge-charge curves of γ'-V_2O_5 during cycling at C/5 rate. 1.6 V - 0.7 V voltage window.2.5M Li_2SO_4-3.5M $ZnSO_4$ electrolyte

Figure S5. Typical discharge-charge curves of γ'-V_2O_5 at different C-rates after 10 activation cycles at C/5. 1.6 V - 0.7 V voltage window. 2.5M Li_2SO_4-3.5M $ZnSO_4$ electrolyte

Figure S6. Discharge-charge curves of γ'-V_2O_5 during cycling at C/5 rate. 1.6 V - 0.7 V voltage window. 3.5M $ZnSO_4$ electrolyte

Figure S7. (a) XRD patterns and (b) Raman spectra of initial γ'-V_2O_5 electrode, after the first discharge and after the first discharge-charge cycle. Stars correspond to the sample holder (stainless steel) reflections. 1C rate. 1.6 V - 0.7 V voltage window

Figure S8. (a) XRD patterns and (b) Raman spectra of initial γ'-V_2O_5 and after cycle tests. *: sample holder (stainless steel) reflections. **+**: new phase. 1C rate. 1.6 V - 0.7 V voltage window

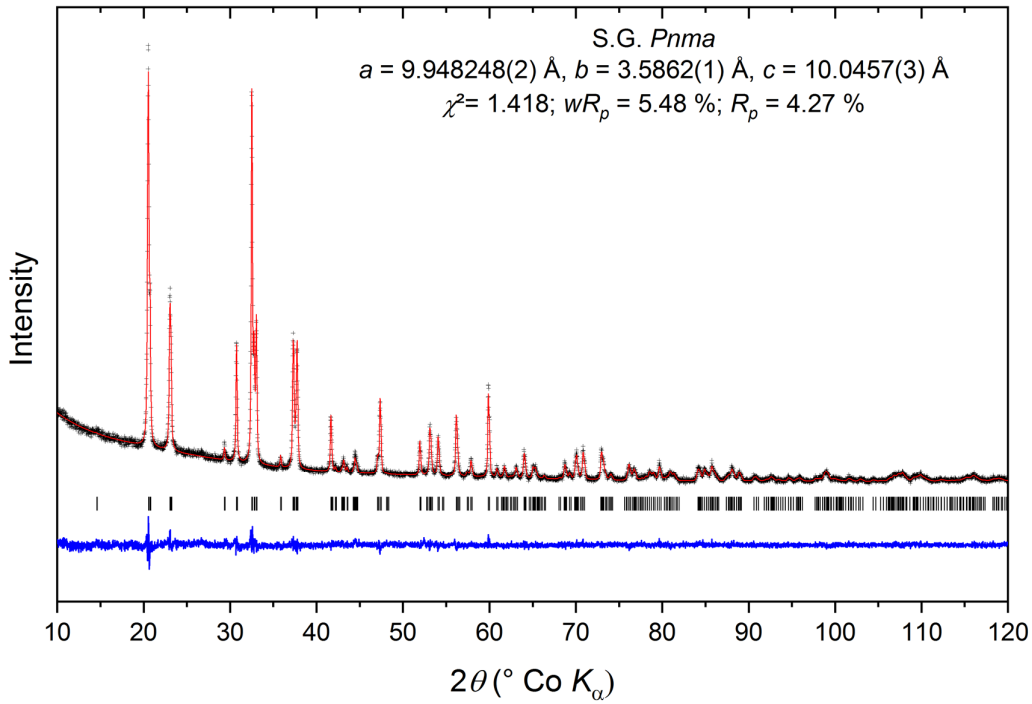

Fig. S1. Rietveld refinement of γ'-V_2O_5 XRD pattern

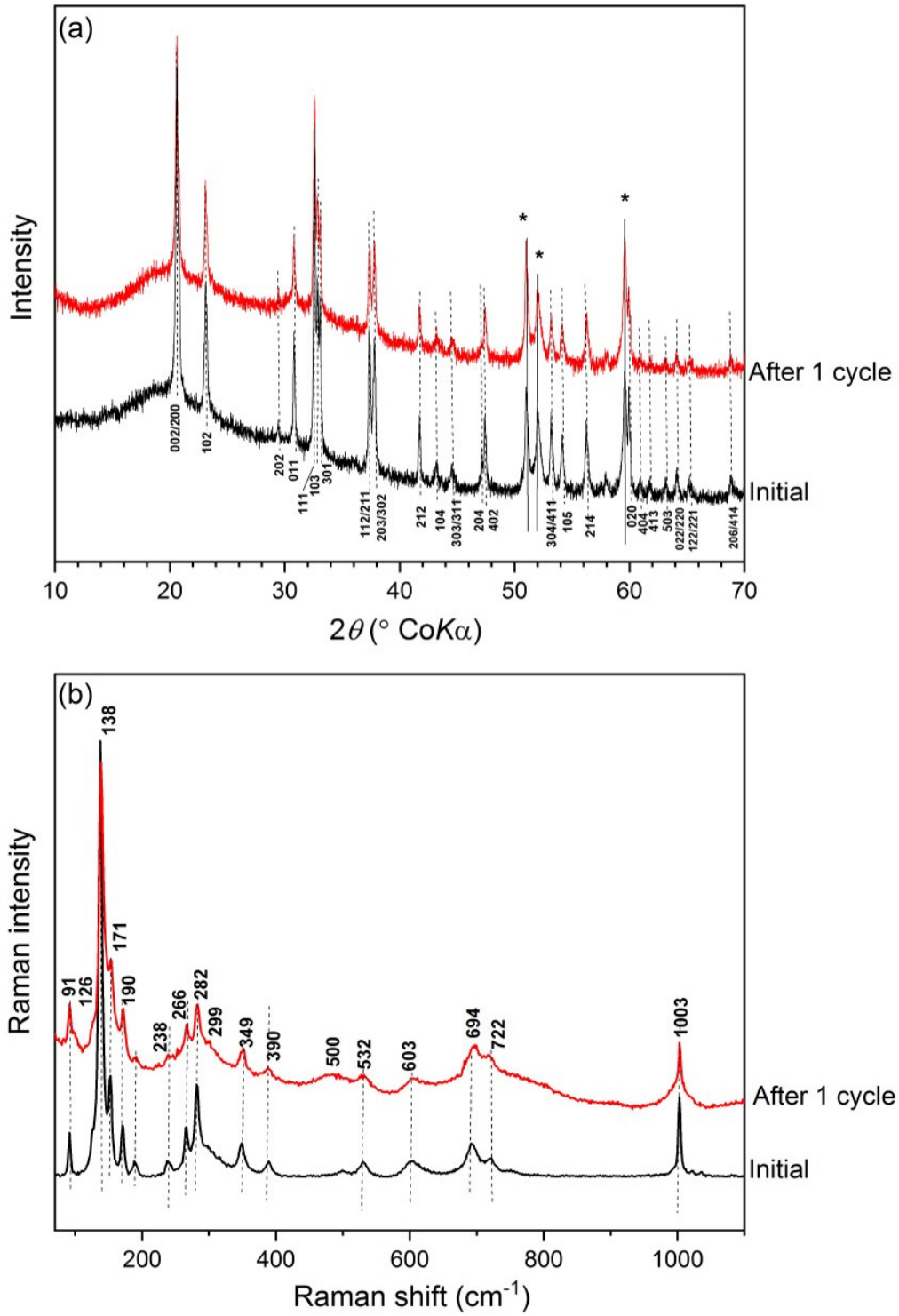

Fig. S2. (a) XRD patterns and (b) Raman spectra of initial γ'-V_2O_5 electrode and after one discharge-charge cycle at C/5 rate. 1.6 V - 1 V voltage window. *: sample holder (stainless steel) reflections

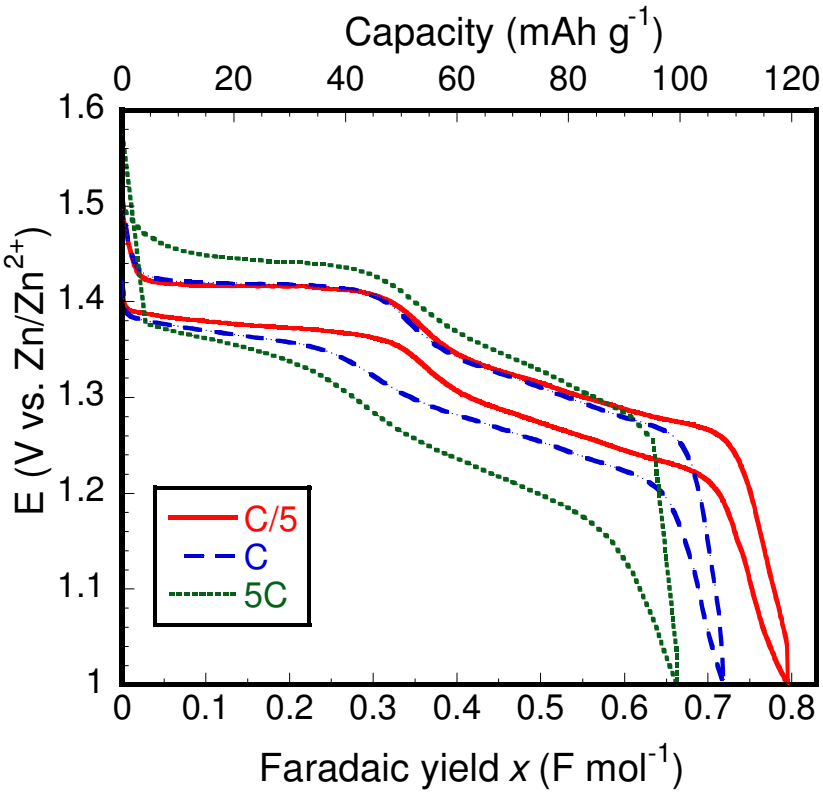

Fig. S3. Influence of the C rate on discharge-charge curves of γ'-V_2O_5. 1.6 V - 1 V voltage window. 2.5M Li_2SO_4-3.5M $ZnSO_4$ electrolyte

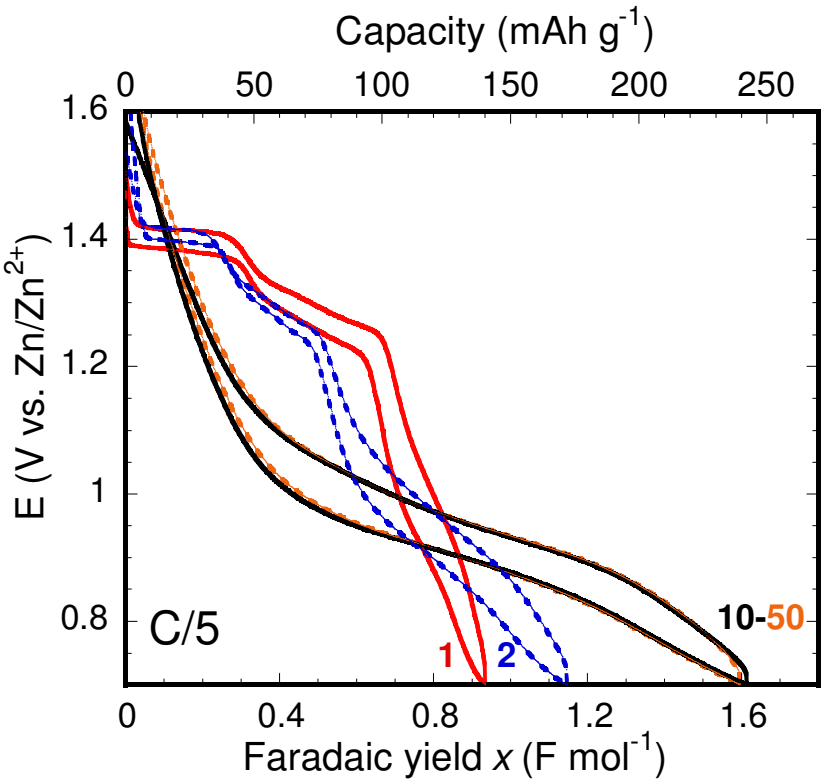

Fig. S4. Discharge-charge curves of γ'-V_2O_5 during cycling at C/5 rate. 1.6 V - 0.7 V voltage window. 2.5M Li_2SO_4-3.5M $ZnSO_4$ electrolyte

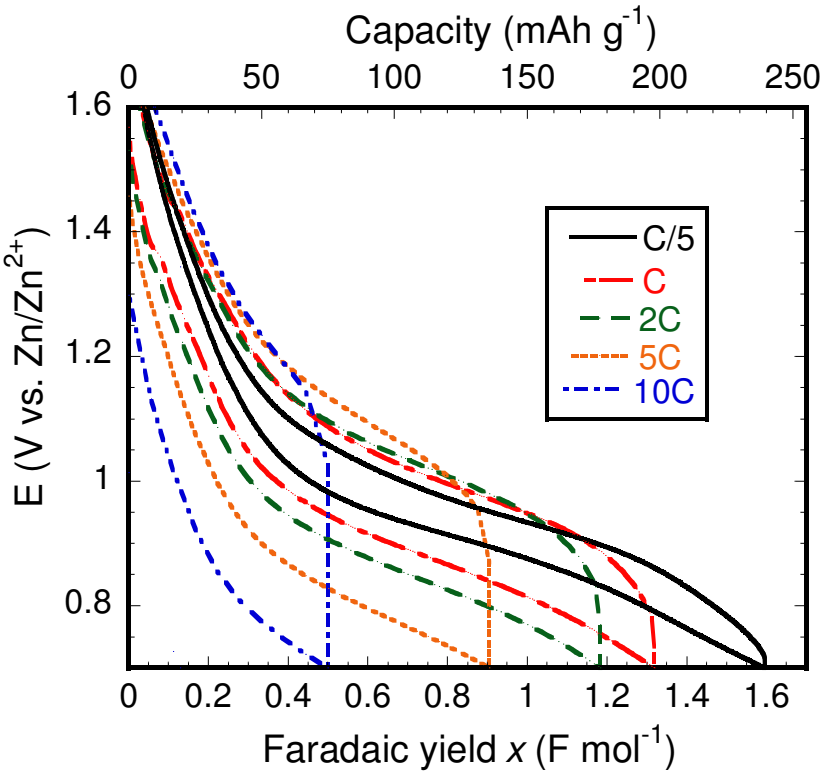

Fig. S5. Typical discharge-charge curves of γ'-V_2O_5 at different C-rates after 10 activation cycles at C/5. 1.6 V - 0.7 V voltage window. 2.5M Li_2SO_4-3.5M $ZnSO_4$ electrolyte

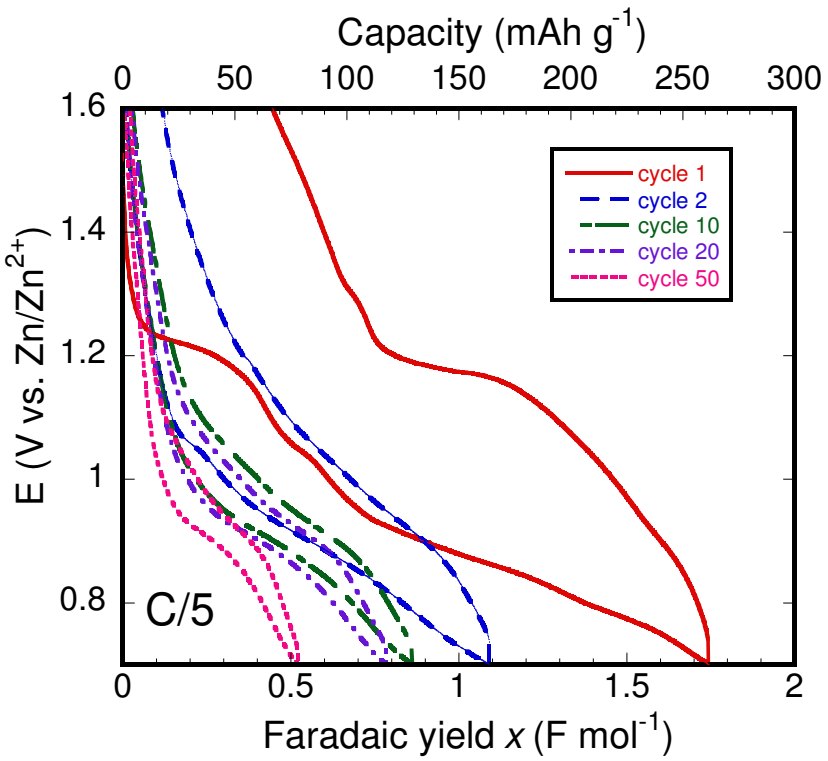

Fig. S6. Discharge-charge curves of γ'-V_2O_5 during cycling at C/5 rate. 1.6 V - 0.7 V voltage window. 3.5M $ZnSO_4$ electrolyte

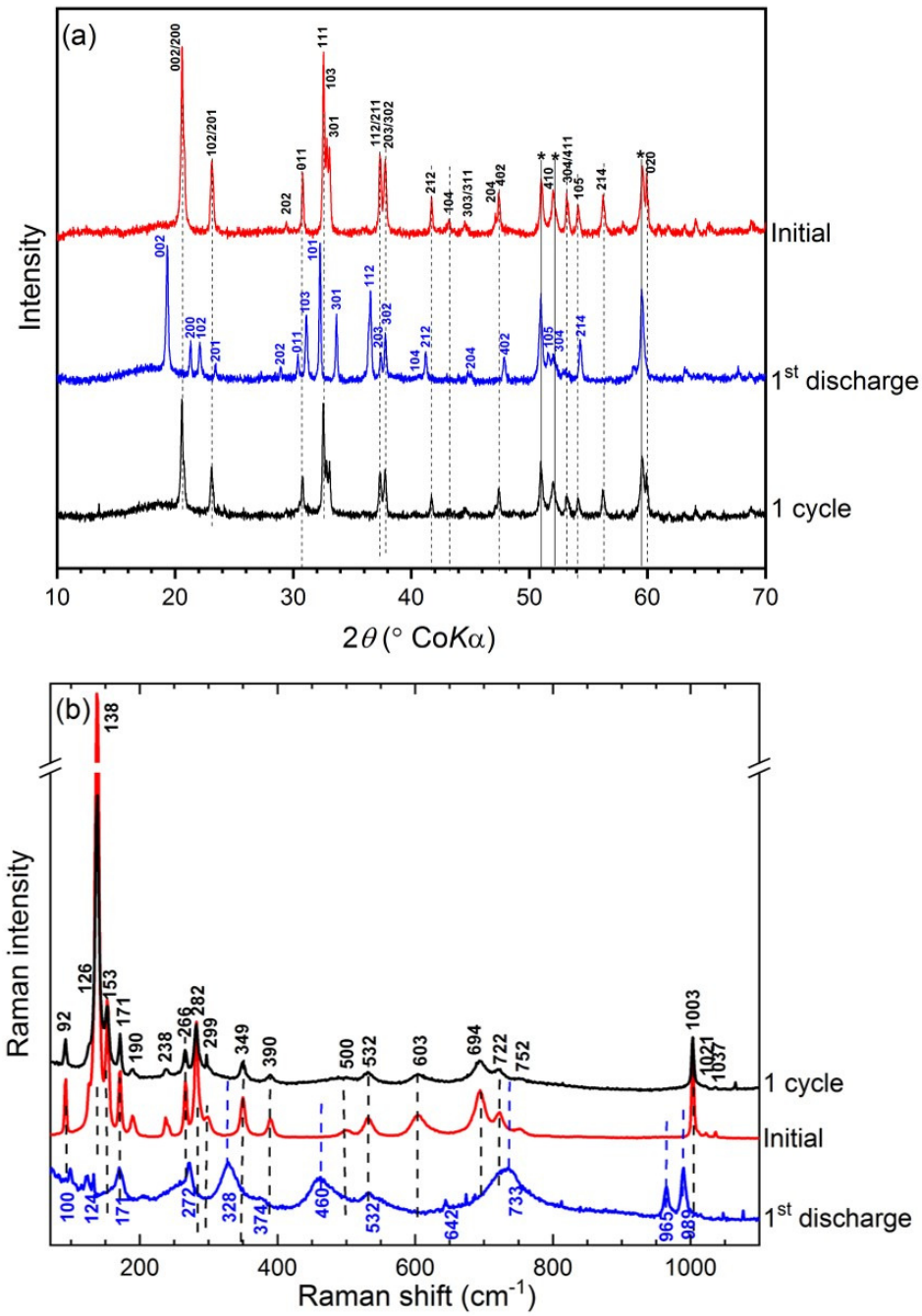

Fig. S7. (a) XRD patterns and (b) Raman spectra of initial γ'-V_2O_5 electrode, after the first discharge and after the first discharge-charge cycle. *: sample holder (stainless steel) reflections. 1C rate. 1.6 V - 0.7 V voltage window

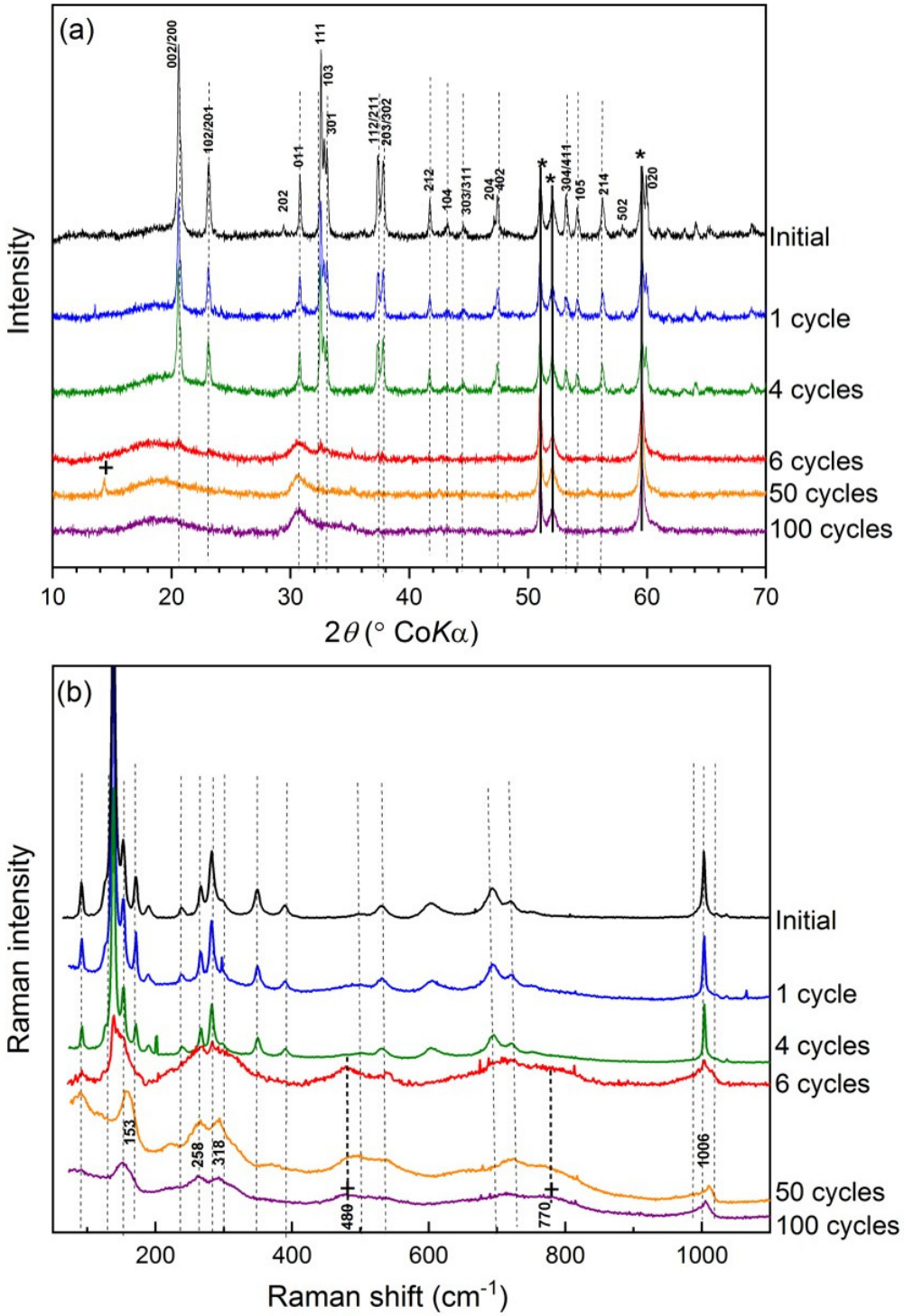

Fig. S8. (a) XRD patterns and (b) Raman spectra of initial γ'-V_2O_5 and after cycle tests. *: sample holder (stainless steel) reflections. **+**: new phase. 1C rate. 1.6 V - 0.7 V voltage window